Marine control over negative power law scaling of mass wasting events in chalk sea cliffs with implications for future recession under the UKCP09 medium emission scenario

Article (Accepted Version)

Marine control over negative power law scaling of mass wasting events in chalk sea cliffs with implications for future recession under the UKCP09 medium emission scenario

Jamie Gilham, John Barlow, and Roger Moore

Department of Geography, University of Sussex, Brighton, UK

Abstract

Coastal cliff erosion represents a significant geohazard for people and infrastructure. Forecasting future erosion rates is therefore of critical importance to ensuring the resiliency of coastal communities. We use high precision monitoring of chalk cliffs at Telscombe, UK to generate monthly mass movement inventories between August 2016 and July 2017. Frequency-magnitude analysis of our inventories demonstrate negative power law scaling over 7 orders of magnitude and, for the first time, we report statistically significant correlations between significant wave height (H_s) and power law scaling coefficients (r^2 values of 0.497 and 0.590 for β and s respectively). Applying these relationships allows for a quantitative method to predict erosion at the site based on H_s probabilities and sea level forecasts derived from the UKCP09 medium emission climate model (A1B). Monte-Carlo simulations indicate a range of possible erosion scenarios over 70 years (2020-2090) and we assess the impact these may have on the A259 coastal road which runs proximal to the cliffs. Results indicate a small acceleration in erosion compared to those based on current conditions with the most likely scenario at the site being 21.7 m of cliff recession by 2090. However, low-probability events can result in recession an order of magnitude higher in some scenarios. In the absence of negative feedbacks, we estimate an ~11% chance that the A259 will be breached by coastal erosion by 2090.

Keywords: Cliff recession, power law scaling, numerical modelling

Introduction

The evolution of sea cliffs has received greater attention in the research literature since the turn of the century (e.g. Lee et al., 2001; Trenhaile, 2002; Dong & Guzzetti, 2005; Teixeira, 2006; Marques, 2008; Lim et al., 2010; Hurst et al., 2016). However, decadal scale ~~quantitative~~ prediction of coastal erosion in response to changing environmental controls ~~over decadal time scales~~ remains a major research objective (Wong et al., 2014). Sea cliff environments are more dynamic than terrestrial slopes due to exogenic forcing from both sub-aerial and marine processes. These, in conjunction with material properties, control the evolution of sea cliffs (Emery & Kuhn, 1982; Lim et al., 2010). Although the mechanical properties of rock slopes are well understood (e.g. Selby, 1993; Wyllie & Mah, 2004; Stead & Coggan, 2012), deterministic approaches become impractical over large spatial and temporal scales due to the difficulties involved in parameterising the sub-surface and in predicting the variability of environmental controls (e.g. Stead & Coggan, 2012). Therefore, an alternate approach is required involving empirically-based stochastic models which extrapolate limited observations over spatial and temporal scales more applicable to landscape evolution (Barlow et al., 2012). Most estimates of future sea cliff erosion are based on change detection between historical maps and aerial photographs (e.g. Moore et al., 2003a; 2003b; Dornbusch et al., 2008). However, this approach is problematic in that measured recession rates are often similar to the precision of the data and extrapolating rates forward in time assumes erosion will not be influenced by projected changes in exogenic boundary conditions (Rosser at al., 2005; Lim et al., 2010). The ability to conduct high-precision monitoring through terrestrial or airborne laser scanning (TLS or ALS) and more recently through UAV photogrammetry has

50 greatly improved the precision of coastal erosion data (Slatton et al., 2007; Remondino
51 et al., 2011; Haala & Rothermel, 2012; Hugenholtz et al., 2013; Gonçalves &
52 Henriques, 2015). However, linking cliff erosion to environmental conditions remains
53 difficult as mass wasting events often occur through progressive failure such that
54 triggering events and failure do not necessarily correlate though time (Lim et al., 2010;
55 de Vilder et al., 2017).

56 Magnitude-frequency analysis is a statistical method for characterising
57 geomorphic events in space and time (Wolman & Miller, 1960; Stark & Guzzetti, 2009).
58 A substantial amount of research has been undertaken on the methods and
59 characteristics of landslide magnitude-frequency distributions (e.g. Hovius et al., 1997,
60 1998, 2000; Pelletier et al., 1997; Stark & Hovius, 2001; Guzzetti et al., 2002; Martin
61 et al., 2002; Hergarten, 2003; Malamud, 2004; Van Den Eeckhaut et al., 2007; Brunetti
62 et al., 2009; Rossi et al., 2010). Mathematically, these studies have demonstrated that
63 a negative power law best describes landslide magnitude-frequency distributions,
64 generally expressed as (Brunetti et al., 2009):

65 $$f(V_R)=sV_R^{-\beta} \quad (1)$$

66 where $f(V_R)$ is the frequency density, V_R is the magnitude of a given event and s and
67 β are empirically derived scaling parameters. Many authors have noted the variability
68 of negative power law scaling parameters due to regional characteristics such as
69 structural geology, morphology, hydrology and climate (Stark & Hovius, 2001;
70 Dussauge et al., 2003; Brardinoni & Church, 2004; Guthrie & Evans, 2004; Malamud
71 et al., 2004; Dong & Guzzetti, 2005; Van Den Eeckhaut et al., 2007; White et al., 2008;
72 Marques, 2008; Brunetti et al., 2009; Rossi et al., 2010; Barlow et al., 2012). However,
73 establishing a numerical link between the scaling parameters and environmental

conditions represents a significant challenge in applying power law statistics to predictive models of landscape evolution (Barlow et al., 2012).

The frequency of failure events along coastal cliffs is generally much higher than that of terrestrial cliffs making them ideal for magnitude-frequency analysis. This research assesses the erosion of chalk cliffs at Telscombe, UK using an inventory of mass movements derived from 12 months of high-precision monitoring. The cliffs are predominantly composed of Newhaven Chalk, which is mechanically weak. High-magnitude instability within the chalk is controlled by sliding across two key joint sets such that a wedge-type failure mechanism is common (Mortimore et al., 2004a; Barlow et al., 2017). Wave attack at the base of cliff influences stability both through direct erosion and through microseismic accelerations. Brain et al. (2014) demonstrated that microseimic shaking induced by storm waves can exceed the strength properties of weaker rocks in areas of high stress concentration. More recently, Earlie et al. (2015) observed that high-magnitude waves can cause ground accelerations an order of magnitude greater than have previously been observed and rates of erosion two orders of magnitude larger than the time-averaged mean for cliffs formed of mudstones, siltstones, and sandstones. The shear strength of joints is significantly influenced by the presence of co-planar rock bridges (Bonilla-Sierra et al., 2015). These results suggest that crack nucleation and progressive failure of rock bridges is likely accelerated due to microseismic shaking associated with high-magnitude storm waves. We hypothesise that the weakness of the chalk combined with the structural control and microseismic accelerations associated with high-magnitude storm waves act to minimise the time of progressive failure. Observations over long sections of cliff that include multiple potential failure blocks should therefore provide a quantitative link between mass movements and wave action at the base of cliff. Indeed, this research

aims to provide a constraint for the power law parameters so that future erosion at Telscombe can be determined using probabilistic erosion models. These models are based on the current and future marine projections provided by the UKCP09 medium emission forecast between 2020 and 2090 and account for sea level rise through a time of exposure approach. Our method is applicable to any coastal cliffs composed of weak rock that respond quickly to basal erosion. Results provide a probabilistic recession model that should be of great use to coastal managers.

Study site

Telscombe cliffs are located along the southeast coast of the UK as shown in Figure 1 and represent one of the few sections of sea cliff between Brighton and Newhaven

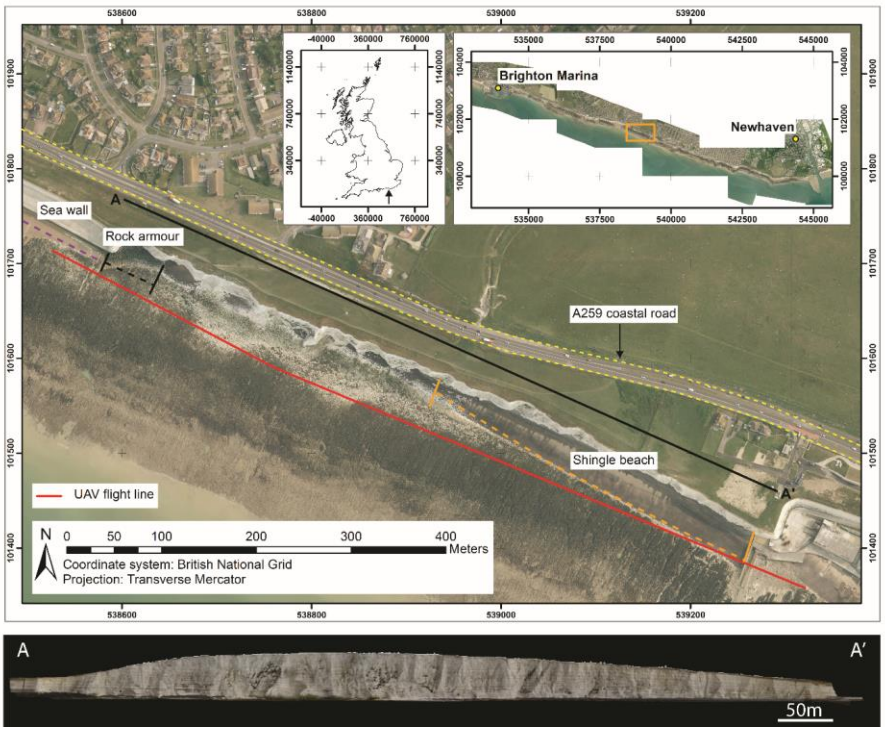

Figure 1: Study area at Telscombe, UK with natural and artificial cliff toe protection identified and cliff model produced through photogrammetry (2013 aerial imagery downloaded from the Channel Coastal Observatory CCO).

that remains undefended. The main coastal road (A259) runs within 42.1m of the cliff edge with an average monthly traffic flow of 21,450 vehicles between 2013 and 2016 (Brighton & Hove City Council, 2017). Formed of Cretaceous Chalk of the Newhaven and Culver formations, the cliffs are approximately 750 m in length with dry valleys at either end of the site (Mortimore, 1997). The maximum elevation is approximately 49 m and the cliffs are orientated towards the dominant wave direction from the south-west (May, 2003). To the west the cliffs have been decoupled from wave action through construction of a sea wall and promenade and have been artificially regraded. Rock armour protects the toe of the cliff for the western 50 m of the site to prevent outflanking of the sea wall (Figure 1). At the eastern extremity a concrete groyne which protects the sewage outfall pipe acts as a barrier to the transport of sediment. As a result, a substantial shingle beach protects the toe of the cliff which tapers over approximately 300 m (Figure 1). The site is macro-tidal with an average spring tidal range of 6.1 m (CCO, 2015) which submerges the shore platform at high tide and enables wave interaction with the base of cliff on a daily basis along the exposed section. Where the cliff is protected by the shingle beach wave interaction occurs during storm events for approximately the western 50-100m when the shingle has been removed from the foreshore. For the remaining section of cliff line the shingle beach remains and therefore wave interaction for this section is minimal. Annual rainfall averages at 720 mm and significant wave heights for this section of coast average at 0.64 m and 1.04 m for the summer and winter months respectively (CCO, 2015). Kinematic analysis of the chalk at the site indicates two steeply inclined joint sets as illustrated in Figure 2 (Barlow et al., 2017). The orientation of these relative to the strike of the cliff face indicates wedge failure as the most likely mode of slope instability. These structural controls produce the characteristic pyramidal morphology

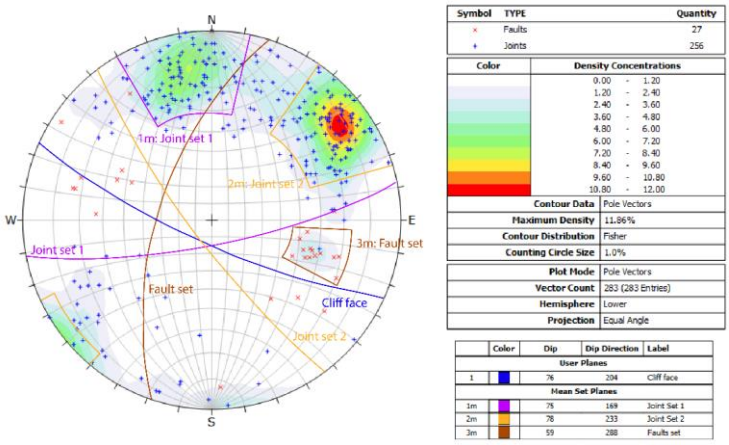

Figure 2: Wolf equal angle stereographic projection of discontinuity data from Telscombe cliffs showing pole plot densities of mapped joints and faults.

of Newhaven formation cliffs (Mortimore et al., 2004a). When saturated, Newhaven Chalk has a cohesion of 600 KN/m^2 and an angle of internal friction of 24º which increase to 2400 KN/m^2 and 43.5º respectively when dry (Mortimore et al., 2004b). This weakness suggests that the chalk will respond quickly to changes in the stress environment brought on by wave erosion.

Methods

This study utilises UAV photogrammetry to populate monthly mass movement inventories based on change detection between sequential 3D cliff models. The resultant magnitude-frequency data were used to develop negative power law models whose paramaters s and β were correlated with H_s. The probability of the maximum failure volume in any given month was used to complete the methodology. Each method and parameter is explained in the following sections.

UAV photogrammetry for obtaining a rockfall inventory

High precision monitoring of the site was conducted using a DJI S1000 octocopter, fitted with a Nikon D810 FX DSLR 36 mega-pixel camera with an AF Nikkor 24mm f/2.8D lens. The camera settings were optimised for the aircraft speed; aperture f/8 and shutter speed of 0.002 (1/5000) sec and natural lighting conditions ISO ranged from 800-1600, over the twelve surveys. An automated flight path was used for each survey which maintained a distance of 50 m between cliff face and the camera with a flying altitude of 21 m (approx. mid-cliff height). During the flights, the camera was maintained orthogonal to the cliff face via live streaming onboard video. A traditional strip plan was selected as the best method of capture for long stretches of cliff line captured from a relatively close distance with short focal length (Birch, 2006). Flight speed was set at 3 ms^{-1} with an image capture interval of 5 s such that an image was captured every 15 m. Initial surveys utilised a ground control network of 23 points located using differential global positioning system and total station surveys. Following the initial surveys, a network of flints was selected and their coordinates extracted from the models to form a relative control network which reduced the field surveying time. Survey accuracy produced a 3D standard error of 0.05 m. Bundle adjustments, generation of epipolar images and point cloud generation was undertaken in the ADAM 3DM software environment. Point clouds which had an average density of 351 points/m^2 were then rasterised to a cell size of 0.1m before a 2.5D change detection (Rosser et al., 2005) was undertaken between successive datasets. The 2.5D change detection was undertaken using the average plane of the cliff which was recorded at 204°. Sub-sections of the study area were investigated and showed ±4°, the impact on the results would considered to be negligible, therefore only one plane was used in all subsequent 2.5D change detection analysis. Error assessment found the greatest component residual error from any monthly dataset was 0.10m, as a result volumetric

estimations were calculated with a minimum reliable detectable rockfall size of 1 x 10^{-3} m^3. A total of 10,085 failures were recorded over the 12 months.

Negative power law parameter estimation

Magnitude-frequency histograms were plotted on logarithmic axes (Figure 3A) using logarithmic binning methods (Guzetti et al., 2002; White et al., 2008; Barlow et al., 2012). Frequency densities were calculated for each bin by using the formula (Malamud et al., 2004):

$$f(V_R) = \frac{\delta N_R}{\delta V_R} \quad (2)$$

where $f(V_R)$ is the frequency density of events with magnitude V_R, δN_R is the number of rockfalls within the specified volume range of δV_R, and δV_R corresponds to the width of the bin. The power law parameters were found using least squares regression (LSR)

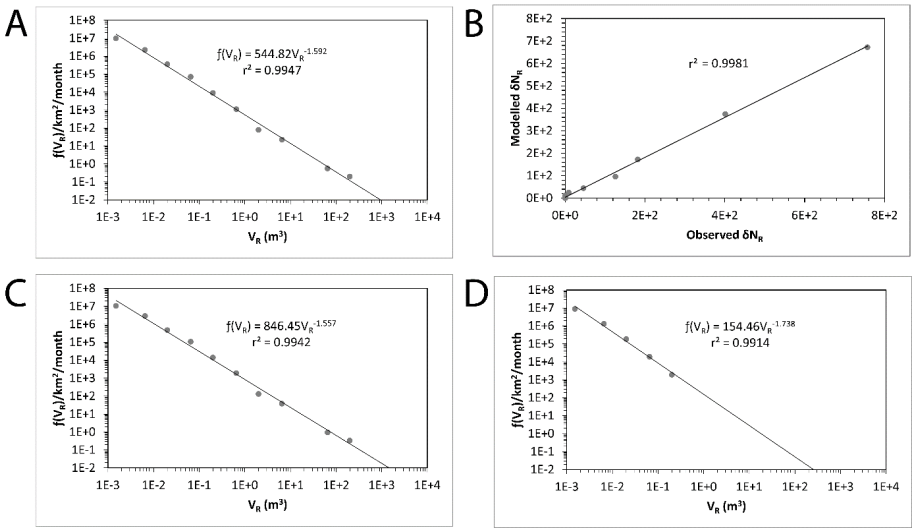

Figure 3: Power law estimation parameters for August to September 2016 (A) frequency density and magnitude of failures for the entire study area, (B) the predicted vs. observed frequency of failures for all binned data, (C) frequency density and magnitude of failures for the undefended section and (D) frequency density and magnitude of failures for the natural defended section (shingle beach) [black lines depict best fit models].

on the logarithmically transformed data (Hovius et al., 1997; Korup, 2005; Barlow et al., 2012). Modelled frequencies were compared to those observed following Barlow et al. (2012) using the integral of Equation 1:

$$\delta N_R = \int_{min}^{max} s V_R^{-\beta} \, dV_R \quad (3)$$

$$\delta N_R = \frac{s V_{R\,max}^{1-\beta}}{1-\beta} - \frac{s V_{R\,min}^{1-\beta}}{1-\beta} \quad (4)$$

By using Equation 4 and setting the $V_{R\,max}$ and $V_{R\,min}$ to the bin widths it is possible to assess the accuracy of the estimated power law parameters against the actual observations (Barlow et al., 2012), an example taken from the month August to September 2016 is provided in Figure 3B. The r^2 value of 0.9981 shows definitive agreement between the observations and the power law model providing confidence that modelled frequencies are reliable. As the period between surveys varied, the frequency densities were normalised by time and area (km^{-2} $month^{-1}$), with a month represented by 30.4375 days (365.25 days per year / 12 months). The study area was subdivided into 'undefended' and 'naturally defended' to account for the impact of the shingle beach on the power law estimations (E.g. Aug- Sep undefended - Figure 3C & naturally defended – Figure 3D) and subsequent analyses. The r^2 values for the power law estimation parameters (E.g. Figure 3A) varied from 0.9697 to 0.9947 for the entire study area, 0.9693 to 0.9942 for the undefended section and 0.9042 to 0.9979 for the naturally defended section (Table 1).

	Entire study area			**Undefended (no beach)**			Naturally defended (beach)		
Month	β	s	r^2	**β**	**s**	**r^2**	β	s	r^2
Aug – Sep 2016	1.592	544.82	0.9947	**1.557**	**846.45**	**0.9942**	1.738	154.46	0.9914
Sep – Oct 2016	1.636	175.20	0.9916	**1.605**	**283.91**	**0.9180**	1.546	110.79	0.9879
Oct – Nov 2016	1.573	369.35	0.9984	**1.565**	**613.84**	**0.9885**	1.455	93.79	0.9922
Nov – Dec 2016	1.471	487.50	0.9870	**1.453**	**780.68**	**0.9868**	1.481	167.47	0.9816
Dec – Jan 2017	1.606	265.07	0.9930	**1.597**	**444.46**	**0.9929**	1.452	84.68	0.9979
Jan – Feb 2017	1.645	460.92	0.9875	**1.606**	**782.57**	**0.9861**	1.745	105.46	0.9834
Feb – Mar 2017	1.421	904.14	0.9881	**1.409**	**1459.50**	**0.9883**	1.150	885.55	0.9668
Mar – Apr 2017	1.697	188.83	0.9701	**1.682**	**318.75**	**0.9693**	1.565	53.37	0.9894
Apr – May 2017	1.680	209.69	0.9697	**1.669**	**330.92**	**0.9724**	1.325	255.91	0.9731
May – Jun 2017	1.955	67.76	0.9811	**1.829**	**139.33**	**0.9805**	2.089	28.25	0.9678
Jun – Jul 2017	1.914	33.79	0.9806	**1.845**	**59.36**	**0.9866**	1.300	716.88	0.9042

Table 1: Power law estimation parameters for Telscombe cliffs (Bold identifies those used for the probabilistic modelling).

Modeling cliff erosion with H_s and sea level rise (SLR)

Erosional flux can be calculated for a given magnitude of event by multiplying the frequency density of the event by the magnitude, the result of applying this to the power law equation is (Barlow et al., 2012):

$$V_{RC} = sV_R^{-\beta} V_R \quad (5)$$

$$V_{RC} = sV_R^{-\beta+1} \quad (6)$$

where V_{RC} is the volume in $m^3\ km^{-2}\ month^{-1}$ for an event of magnitude V_R. Thus, the total volumetric erosional flux (V_T) of rock between a minimum and maximum magnitude can be calculated by (Barlow et al., 2012):

$$V_T = \int_{min}^{max} sV_R^{-\beta+1}\, dV_R \quad (7)$$

$$V_T = \frac{sV_{R\,max}^{2-\beta}}{2-\beta} - \frac{sV_{R\,min}^{2-\beta}}{2-\beta} \quad (8)$$

The maximum volume ($V_{R\,max}$) for Equation 8 can be easily extracted from the rockfall inventory, the minimum value can be more difficult to determine. The minimum detectable rockfall volume using our method was $1 \times 10^{-3}\ m^3$. To avoid data censoring of smaller volumes (e.g. Stark & Hovius, 2001), a value of $1 \times 10^{-6} m^3$ was used as the minimum threshold in Equation 8.

The distribution of the monthly power law scaling parameters was tested for correlation with H_s, temperature, precipitation, and wind speed data. The atmospheric data was downloaded from the Brighton Marina meteorological station (CCO, 2017a) and the wave data from the distal wave buoy at Seaford, approx. 8.5km from Telscombe at a depth of 11 m CD provided by the Channel Coastal Observatory (CCO, 2017b). To determine the waves which interact with the base of cliff the minimum elevation of the cliff toe was extracted from the photogrammetry models. Tidal data downloaded from the British Oceanographic Centre (BODC, 2017) for Newhaven enabled a binary classification of tidal interaction with the base of cliff. This

classification was then applied to the dataset so only waves which interacted with the cliff were considered in the analysis.

The projections of future wave climate are presented by the UKCP09 (Lowe et al., 2009) and were generated using the medium emission scenario (IPCC scenario A1B, Leake et al., 2009). This scenario was chosen as it represents the model which global climate change is most closely following (DEFRA, 2009). The wave model was run for the UK continental shelf and meteorological parameters of wind and pressure obtained from the Hadley Centre Met Office were used to force the wave and surge models (Brown et al., 2012). The regional model was divided into approximate 12km grid cells, with the nearest to the study site selected for data extraction. This grid cell was considered an appropriate level of detail for the modelling as it represents a comparable distance between the study site and the distal wave buoy (8.5km). The wave climate is therefore assumed to be representative of the area. A detailed explanation of the wave model and data generation is provided by Brown et al. (2012). The 6-h time series dataset was grouped by month and averaged over 20 years to obtain each decade (e.g. 2010-2029 generates the decade 2020-2029) as is the case with all UKCP09 sub-aerial and marine projections. Probability plots were obtained for each month in each decade between January 2020 and December 2089 (e.g. Figure 4) and a relationship between probability and H_s was found for each month. Random number generation between 0 and 1 could then be used to obtain a H_s value which would calculate β and s using relationships discussed below~~later~~. To account for SLR the percentage of the tidal cycle that interacts with the base of cliff was recorded, under present conditions 28.58% of the tidal cycle is at or above the minimum cliff height. Using the relative sea level (RSL) rise data presented by the UKCP09 (Lowe et al., 2009), under the medium emission scenario, the 50th percentile

(most likely scenario)

Commented [jb1]: Formatting issue here

was

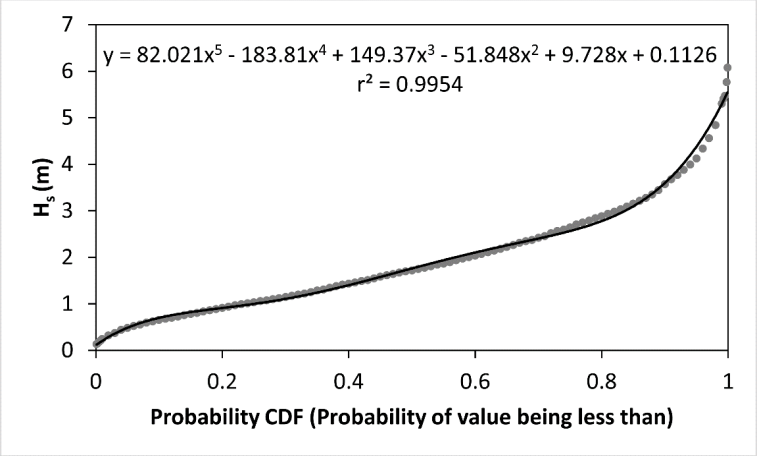

Figure 4: Example of H_s vs. cumulative distribution probability (CDF).

extracted for each year. This increase in sea level was added to the observed data and reflected as a percentage of the tidal cycle which interacted with the cliff. From the current observations to 2090 there is a predicted increase from 28.58% to 33.85%. To reflect this in the model the total volume (V_T) calculated from Equation 8 under current conditions whereby 28.58% of the tidal cycle interacts with the cliff was given a scaling factor of 1. The yearly increase in sea level was then given a scaling factor relative to this base level. Therefore, by 2090 when there is a predicted increase of 5.27% in the percentage of the tidal cycle interacting with the cliff, the scaling factor applied to V_T for that year was 1.0527.

For the $V_{R\ max,}$ values, a cumulative probability plot was generated (Figure 5) from the inventory so that a random number between 0 and 1 could generate a maximum failure volume to be used in Equation 8. As no single model accurately expressed the relationship between cumulative probability and maximum failure, two logarithmic relationships were selected (intersect when cumulative probability = 0.822).

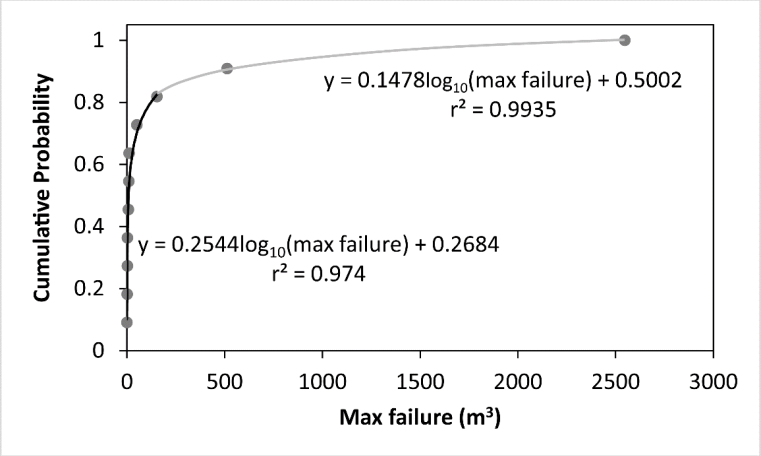

Figure 5: Cumulative probability plot for max failure (black and grey lines indicate best fit models.

Using the numerical relationships presented a Monte Carlo simulation model was run based on Equation 8. To determine the most likely erosion scenario, 10,000 iterations of the model were run from 2020-2090 (70 years). Comparisons between the model outputs and historical recession rates were undertaken to assess model reliability. The V_T for 2020-2090 under current conditions, maintained for the entire temporal period, and future conditions as discussed were then used to calculate cliff top recession which enabled an assessment of the risk to the A259 coastal road for this time period.

Model validation

We validated our initial model results by plotting the observed V_T against the modelled V_T. The r^2 value for the undefended section was very strong at 0.9918 and the model predicted 97% of the observed V_T for this section. The model performs well with respect to the months with the largest failures and the model overestimates V_T when the total volumetric flux for a given month is less than approximately 10 m^3 as also reported by Barlow et al. (2012). The undefended section produced the stronger model with respect to H_s as the neighbouring section of cliff with the natural beach

offered substantial protection from wave action affecting the toe, and therefore the monthly erosion (V_T) of the naturally defended cliff section was significantly reduced (Table 2).

Orthorectification of aerial images from 1957, 1973, 1991 and 2013 of the study area was undertaken using photogrammetric methods. Historical recession rates were calculated using the ArcGIS extension - Digital Shoreline Analysis System (DSAS) developed by the United States Geological Society (Thieler et al., 2009). The model predicts average annual recession under current conditions of 0.29m yr^{-1}, the historical recession rate obtained from the orthorectified imagery between 1957 and 2013 for the same area was 0.31m yr^{-1} ±0.16m (2σ) which is similar to other published retreat rates for the site in the scientific literature (Dornbusch et al., 2008). The similarity of the results using different methods of calculating cliff recession provides greater confidence in the model output. The subsequent analysis therefore focusses on the undefended section of cliff line.

Commented [jb2]: Include error

Results and discussion

2.5D surface change detection

Our high-precision monitoring has provided evidence of erosional cycles at the site focused around the conjugate joint sets. Figure 6 illustrates the 2.5D surface change detection results which identify toe erosion between August 2016 (Figure 6A) and February 2017 (Figure 6F) totalling 104.90m^3, concentrated in the lower section of the cliff. As a result of this erosion, the mean slope angle of the cliff face increased from ~76° to ~80.5°. This steepening resulted in a large wedge failure observed in March 2017 (Figure 6G). Over time wave action will remove the debris at the base of cliff and restart the cycle.

328

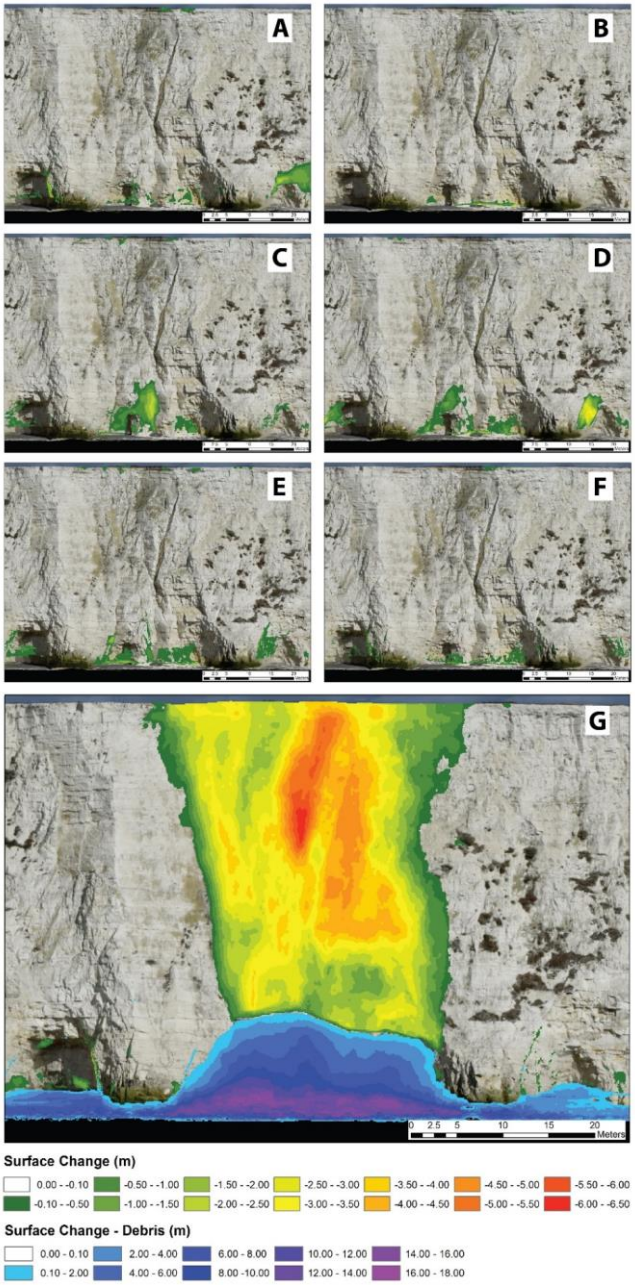

Figure 6: Surface change between August 2016 and March 2017, illustrating a time series of toe erosion and wedge failure (A) Aug-Sep 2016, (B) Sep-Oct 2016, (C) Oct-Nov 2016, (D) Nov-Dec 2016, (E) Dec 2016-Jan 2017, (F) Jan-Feb 2017 and (G) Feb-Mar 2017.

329 **Erosion modelling**

330 We sampled mass movements across 7 orders of magnitude. Given that the
331 largest event in our inventory involved the entire rock face at the highest point in the
332 cliffs, we are confident that we have data covering the entire range of failure
333 magnitudes that are possible at the site. The inventory is comprised of 10,085 mass
334 movements with a total volumetric flux of 3,889.35 m^3. The surface area of the cliff
335 face for the entire study area is 23,597.45 m^2, this was subdivided into the undefended
336 section and the naturally defended beach section with surface areas of 13,890.46 m^2
337 and 9,706.99 m^2 respectively. Although accounting for approximately 59% of the
338 study area, the undefended section had a total volumetric flux of 3,872.62 m^3,
339 representing 99.57% of the entire study area total. The monthly inventories are listed
340 in Table 2 and comparisons made between the total volumes (V_T) for the undefended
341 (no beach) and naturally defended (beach) sub-sections. The largest failure was
342 observed between February and March 2017 with an estimated volume of 2,546.81
343 m^3. Other notable failures occurred between November and December 2016 and in
344 the late summer of 2016 (August – September 2016) with estimated volumes of 512.23
345 m^3 and 152.66 m^3 respectively. Correlations can be drawn between these larger
346 failures and the distal wave environment of the period between surveys. The average
347 H_s for Aug-Sep, Nov-Dec and Feb-Mar were 1.26 m, 2.12 m and 2.31 m respectively.
348 Furthermore, the percentage of waves which interacted with the cliff that were
349 classified as distal storm waves, H_s > 3.85 m (Bovington et al., 2015), were 6% (Aug-
350 Sep), 9% (Nov-Dec) and 14% (Feb-Mar), the highest percentage in the remainder of
351 the dataset was 3% between May and June. These results indicate a minimal lag time
352 between delivery of high energy waves and large magnitude events, either through

toe erosion or a significant increase in the stress environment propagating along conjugate joints (Sunamura, 2015).

Month	V_T Observed (m^3)	
	Undefended (no beach)	Naturally defended (beach)
Aug – Sep 2016	252.59	2.83
Sep – Oct 2016	22.05	1.23
Oct – Nov 2016	119.16	0.81
Nov – Dec 2016	622.01	1.02
Dec – Jan 2017	64.41	0.47
Jan – Feb 2017	31.42	1.83
Feb – Mar 2017	2702.04	1.59
Mar – Apr 2017	20.07	0.67
Apr – May 2017	32.03	3.79
May – Jun 2017	4.59	1.8
Jun – Jul 2017	2.24	0.69

Table 2: Monthly observed total volumetric erosion (V_T) for the undefended and naturally defended cliff line at Telscombe.

Scaling parameters

Significant linear regression correlations, at the 95.5% (2σ) confidence level, were found between H_s and the β and s values with r^2 values of 0.4971 and 0.5902 respectively for the undefended section of cliff (Figure 7A & 7B). A dataset with a greater spatial extent would likely increase the strength of these relationships as the site has a limited number of conjugate joint sets where wedge failures occur, each at a different stage of the failure cycle. Reoccurring failures are therefore temporally limited by the erosional cycle. With a greater sample of conjugate joint sets the likelihood that delivery of high energy waves would lead to failure is increased, thus strengthening the relationships between H_s and the power law scaling parameters. The linear regression relationship between s and H_s intersects the x axis at 0.602 m for the undefended section (Figure 7B). When comparing the erosion activity to the H_s values from the observation dataset it was considered appropriate to determine that if the value of H_s in the model was below this threshold the erosion activity would be set to zero. AFurthermore a control site at Brighton marina, where the cliffs are

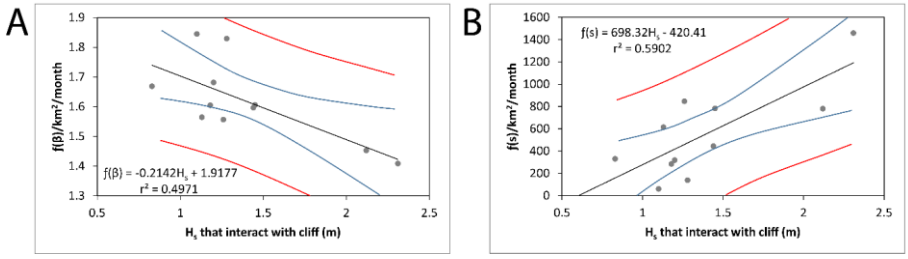

Figure 7: Normalised power law estimation parameters β and s vs. H_s (A) β vs. H_s for the undefended section of cliff and (B) s vs. H_s for the undefended section of cliff (black lines indicate best fit models, blue lines the 95.5% CI and red lines the 95.5% predicted values range).

~~protected~~ disconnected from wave energy by a sea wall, recorded no detectable erosion during the same period. Although sub aerial and marine erosion below the threshold do occur, the influence of these on ~~the~~ total ~~overall~~ mass flux appears to be ~~is likely to be~~ negligable ~~minimal~~. No significant correlation was found between the scaling parameters and wave direction (r^2 values of 0.0884 for β and 0.0293 for s), or sub-aerial conditions of precipitation (r^2 values of 0.0002 for β and 0.0006 for s) and air temperature (r^2 values of 0.2628 for β and 0.2178 for s) for the undefended section. Likewise there were no significant correlations found for the naturally defended beach section for any marine or sub-aerial variables considered.

The s value provides an indication on the level of activity within a given dataset whereas β describes the relative contribution of high-magnitude events to the total volume (Barlow et al., 2012). For example, as β increases, smaller magnitude events contribute a greater amount to the total volume than the larger magnitude failures. The normalised scaling parameters for the undefended section of cliff vary between 1.409 to 1.829 for β and from 59.36 to 1459.50 for s. The range in β values is consistent with those presented in other scientific research (Van Den Eeckhaut et al., 2007; Brunetti et al., 2009; Barlow et al., 2012). The smaller β and larger s values are generally found in the winter months (winter ave. β=1.537, ave. s=895.51, summer

ave. β=1.744, ave. s=348.38) when an increase in erosion would be expected due to the frequency of storms. With regards to the maximum failure volume (V_{max}), this is primarily controlled by the slope morphology (Martin et al., 2002). By finding statistically significant relationships between the scaling parameters (β & s) with Hs the power law model can be constrained to provide a useful predictive capability for future coastal management which is presented in the following section.

Erosion scenarios

Results from our Monte Carlo simulations enabled a comparison between predicted erosion under current conditions and that predicted under UKCP09 conditions. Scaling parameters were controlled through the derived relationships with H_s (Figures 6A & 6B) and the maximum failure volume calculated using the cumulative probability relationships found from the inventory (Figure 5).

The results of the Monte Carlo simulation are provided in Figure 8 and Table 3. The mean total recession increases by 1.31 m (approx.+6%) over the 70 year period

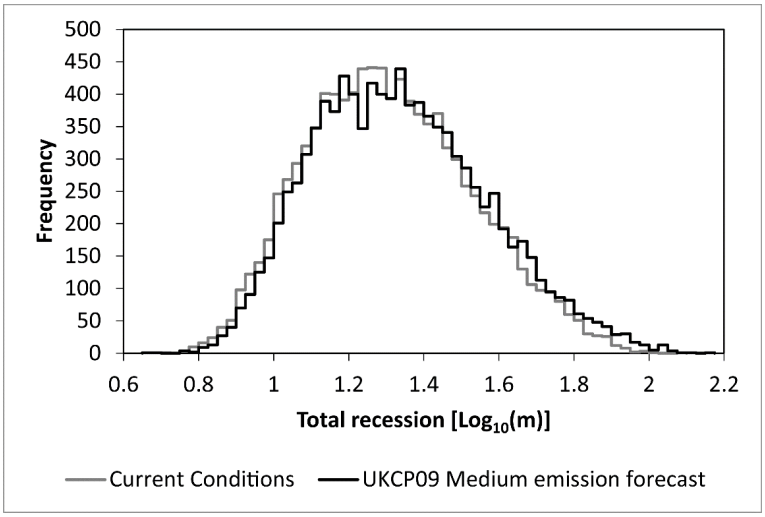

Figure 8: Monte Carlo simulation histogram of Log_{10} transformation of total recession between 2020 and 2090.

between the future and current conditions (Table 3), highlighting the impact of future sea level rise and an increase in significant wave height. The results from the Monte Carlo simulation were normally distributed with a strong positive skew due to the influence of extreme events. In order to apply parametric statistics, the skew was eliminated using a $\log_{10}$ transformation as shown in Figure 8. The maximum recession

Commented [jb3]: Why the big gap here?

distances produced by the model were 121.97 m and 143.56 m under current and future conditions (under the UKCP09 medium emission scenario) respectively. The reason for these extremes values are twofold, firstly due to the high magnitude failure (2546.81 m^3) observed in the February to March 2017, this magnitude of failure can be generated in any month of the simulation due to the cumulative probability relationship (Figure 5). This, in combination with projected increases in H_s, enables the model to predict a monthly V_T several orders of magnitude greater than observed in the inventory during the 70 year simulation. However, it should be noted that for these extreme cases the frequency of occurrence was reported as 1/10,000. As the model was run over a 70 year period, the chance of this extreme event occurring is one in 700,000 years. This corresponds to over three standard deviations from the mean under both current and future conditions, reaffirming the unlikelihood of occurrence. The influence of the extreme events impacts the standard deviation resulting in annual recession uncertainty that is approximately three times greater than the calculated historical recession rates (2σ). However, assessing the range of recession values closer (<2σ) to the mean (Figure 8) reveals a significant chance that recession totals between 30 - 60 m over the 70 year period.

	Current conditions		UKCP09 medium emission forecast	
	Recession Log_{10}(m)	Recession (m)	Recession Log_{10}(m)	Recession (m)
Average	1.311	20.45	1.338	21.76
Max	2.086	121.97	2.157	143.56
Min	0.714	5.18	0.659	4.56
95.5%CI	1.750	56.26	1.797	62.61

Table 3: Results of Monte Carlo simulation.

Formatted Table

447 The distance between the cliff edge and the A259 ranges between 42.07 m to
448 52.75 m with an average of 46.62 m. Under the most likely erosion scenario (mean in
449 Table 3) approximately 56.6% and 59.7% of the area between the cliff line and
450 minimum distance to the road could be lost by 2090 for current and future conditions
451 respectively (Figure 9). Under both modelled scenarios the 95.5% certainty limit
452 breaches the A259 coastal road (Figure 9) and therefore highlights the potential risk
453 to infrastructure if recession exceeds the modelled average. Assessing the minimum
454 distance from the cliff top to the road approximately 8% of model runs would lead to a
455 breach under current conditions, this increases to about 11% accounting for future
456 conditions as illustrated in Figure 10. The results from this analysis indicate that
457 coastal management policies may need to be reviewed with regards to the current
458 position and future risk to the coastal road. As evidenced with neighbouring sections
459 of cliff line when defences have been installed the annual recession rate has
460 decreased by an order of magnitude. Beach growth is a negative feedback to cliff
461 erosion, where recession results in delivery of flint from the cliff to the beach.

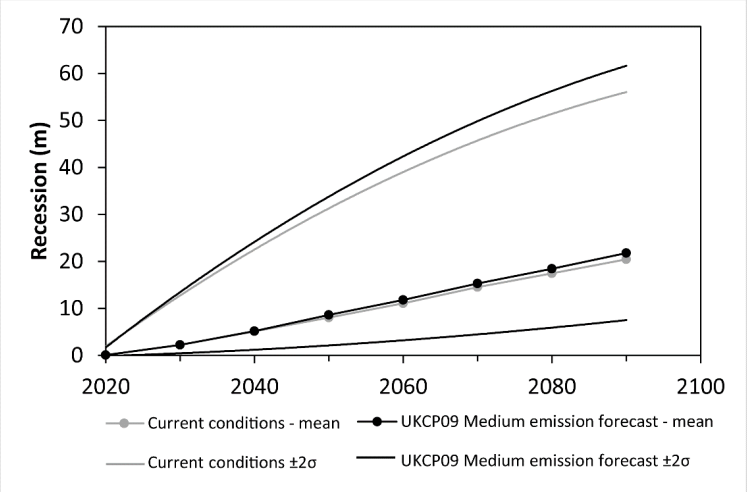

Figure 9: Decadal total cliff recession from Monte Carlo Simulation after 10,000 model runs (Mean recession depicted by data points).

Alternatively accelerated recession within the undefended section could create an embayment and lead to the formation of a pocket beach. The effectiveness of a beach at the cliff toe is evident from the naturally defended section with a significant reduction in erosion (Table 2). The model predictions assume the current state of the site, undefended versus naturally defended (beach), persists into the future.

Commented [jb4]: This bit reads pooly.

Commented [jb5]: Remove the equations from fig 10. We don't use them for anything and they just cloud the issue.

Commented [jb6R5]:

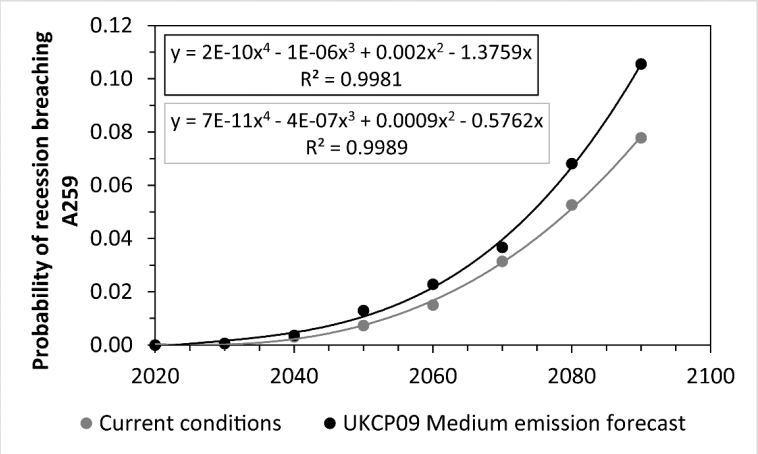

Figure 10: Probability of cliff erosion breaching the A259 at Telscombe cliffs assuming current H_s conditions (grey line) and the UKCP09 forecast for H_s (black line)

Conclusions

This study demonstrates the first statistical link between power law scaling parameters and significant wave height (H_s). ~~-~~This relationship suggests that there is minimal lag between delivery of high energy waves to the base of cliff and failure events. ~~Such relationships offer the potential to quantify the evolution of landscapes under varying environmental boundary conditions.~~ Our results demonstrate the importance of H_s in driving cliff recession at the site and offer the potential to quantify the evolution of landscapes under varying marine conditions. ~~This relationship suggests that there is minimal lag between delivery of high energy waves to the base of cliff and failure events.~~ The simulations involving increased H_s predicted by the UKCP09 model result

in a slight acceleration in cliff recession at the site with the most likely outcome being 21.7 m by 2090. However, the possibility of extreme events within the model is such that the probability of breaching the A259 increases from ~0% in 2020 to ~11% by 2090. The model presented explains ~50% and ~59% of the variation of β and s respectively. Much of the remaining variability is probably controlled by endogenic processes and represents an interesting topic for future research. Although our approach is data hungry, once the inventory data is in place it does not require specialist software to run the simulations such that predictions can be readily updated should improved climate forecasts become available. These methods are transferrable to other sites where the lag between triggering events and mass movement are considered to be minimal. Therefore, our method provides coastal managers with a probabilistic tool to evaluate potential risk to infrastructure through time to facilitate effective planning and mitigation.

Acknowledgements

This research was funded through an EPSRC iCASE Studentship (Engineering and Physical Sciences Research Council Industrial Co-operative Award in Science and Engineering) through the University of Sussex with industrial collaboration from Halcrow Group Ltd (A CH2M Company) reference number: EP/L505687/1. The authors would also like to thank two anonymous reviewers for their comments which have improved this manuscript.

References

ADAM Technology. (2010). *3D Measurement, Camera Calibration and Block Adjustment Software. User's Manual*. Belmont, Australia: ADAM technology.

500 Barlow, J., Gilham, J., & Cofrã, I. I. (2017). Kinematic analysis of sea cliff stability
501 using UAV photogrammetry. *International Journal of Remote Sensing*. DOI:
502 10.1080/01431161.2016.1275061
503 Barlow, J., Lim, M., Rosser., N; Petley, D., Brain, M., Norman, E., & Geer, M. (2012).
504 Modelling cliff erosion using negative power law scaling of rock falls.
505 *Geomorphology*, 139-140, pp. 416-424. DOI: 10.1016/j.geomorph.2011.11.006
506 Birch, J. S. (2006). 'Using 3DM Analyst Mine Mapping Suite for Rock Face
507 Characterization', in Tonon, F., & Kottenstette, J. (Eds.) *Laser and*
508 *Photogrammetric Methods for Rock Face Characterization*. Virginia, USA:
509 American Rock Mechanics Association (ARMA).
510 Bonilla-Sierra, V., Scholtes, L., Donze, F-V., & Elmouttie, M. (2015). DEM analysis
511 frock bridges and the contribution to rock slope stability in the case of
512 translational sliding failures. *International Journal of Rock Mechanics & Mining*
513 *Sciences*, 80, pp 67-78.
514 Bovington, J., Amos, D., & Warman, L. (2015). *Annual Report 2015 – Beachy Head*
515 *to Selsey Bill*. Retrieved from http://www.channelcoast.org/reports/
516 Brardinoni, F., & Church, M. (2004). Representing the landslide magnitude–
517 frequency relation: Capilano River Basin, British Columbia. *Earth Surface*
518 *Processes and Landforms*, 29(1), pp. 115–124. DOI: 10.1002/esp.1029
519 Brain, M. J., Rosser, N. J., Norman. E. C., & Petley, D. N. (2014). Are microseismic
520 ground displacements a significant geomorphic agent? Geomorphology, 207,
521 pp 161–173.
522 Brighton and Hove City Council. (2017). *Travel, transport and road safety: Counting*
523 *traffic in Brighton and Hove.* Retrieved from http://www.brighton-

hove.gov.uk/content/parking-and-travel/travel-transport-and-road-safety/counting-traffic-brighton-and-hove

British Oceanographic Data Centre (BODC). (2017). *UK Tide Gauge Network: Download Data*. Retrieved from: https://www.bodc.ac.uk/data/hosted_data_systems/sea_level/uk_tide_gauge_network/processed_customise_time_selection/

Brown, J.M., Wolf, J., & Souza, A.J. (2012). Past to future extreme events in Liverpool Bay: model projections from 1960-2100. *Climatic Change*, 111(2), pp. 365-391. DOI: 10.1007/s10584-011-0145-2

Brunetti, M.T., Guzzetti, F., & Rossi, M. (2009). Probability distributions of landslide volumes. *Nonlinear Processes in Geophysics*, 16, pp. 179–188. DOI: 10.5194/npg-16-179-2009

CCO (Channel Coastal Observatory). (2015). *Channel Coastal Observatory - Regional Coastal Monitoring Programmes Seaford Wave Buoy*. Retrieved from: http://www.channelcoast.org/data_management/real_time_data/charts/?chart=81andtab=infoanddisp_option=.

CCO (Channel Coastal Observatory). (2017a). *Channel Coastal Observatory - Regional Coastal Monitoring Programmes Brighton Met Station*. Retrieved from: http://www.channelcoast.org/data_management/real_time_data/charts/?chart=88&tab=met&disp_option=

CCO (Channel Coastal Observatory). (2017b). *Channel Coastal Observatory - Regional Coastal Monitoring Programmes Seaford Wave Buoy*. Retrieved from: http://www.channelcoast.org/data_management/real_time_data/charts/?chart=

548 81&tab=waves&start=1504087200&end=1504173600&disp_option=1&datum=
549 chart
550 Department for Environment, Food & Rural Affairs – DEFRA. (2009). *Adapting to*
551 *climate change – UK Climate Projections*. London: DEFRA.
552 de Vilder, S. J., Rosser, N. J., & Brain, M. J. (2017). Forensic analysis of rockfall
553 scars. *Geomorphology*, 295, pp. 202-214. DOI:
554 10.1016/j.geomorph.2017.07.005
555 Dong, P., & Guzzetti, F. (2005). Frequency-size statistics of coastal soft-cliff erosion.
556 *Journal of Waterway, Port, Coastal, and Ocean Engineering, 131(1), pp. 37-42.*
557 Dornbusch, U., Robinson, D. A., Moses, C. A., & Williams, R. B. G. (2008). Temporal
558 and spatial variations of Chalk cliff retreat in East Sussex, 1873 to 2001. *Marine*
559 *Geology*, 249(3-4), pp. 271-282. DOI: 10.1016/j.margeo.2007.12.005
560 Dussauge, C., Grasso, J.-R., & Helmstetter, A. (2003). Statistical analysis of rock fall
561 volume distributions: implications for rock fall dynamics. *Journal of Geophysical*
562 *Research*, 108(B6), 2286. DOI: 10.1029/2001JB000650
563 Earlie, C. S., Young, A. P., Masselink, G., & Russell, P. E. (2015), Coastal cliff
564 ground motions and response to extreme storm waves, Geophys. Res. Lett.,
565 42, pp 847–854. DOI:10.1002/2014GL062534.
566 Emery, K. O., & Kuhn, G. G. (1982). Sea cliffs: their processes, profiles, and
567 classification. Geological Society of America Bulletin, 93, pp.644-654.
568 Gonçalves, J. A., & Henriques, R. (2015). UAV photogrammetry for topographic
569 monitoring of coastal areas. *ISPRS Journal of Photogrammetry and Remote*
570 *Sensing*, 104, pp. 101-111. DOI: 10.1016/j.isprsjprs.2015.02.009

571 Guthrie, R., & Evans, S. (2004). Analysis of landslide frequencies and characteristics
572 in a natural system. Coastal British Columbia. *Earth Surface Processes and*
573 *Landforms*, 29(11), pp. 1321–1339. DOI: 10.1002/esp.1095
574 Guzzetti, F., Malamud, B., Turcotte, D., & Reichenbach, P. (2002). Power-law
575 correlations of landslide areas in central Italy. *Earth and Planetary Science*
576 *Letters*, 195(3-4), pp. 169–183. DOI: 10.1016/S0012-821X(01)00589-1
577 Haala, N., & Rothermel, M. (2012). Dense Multi-Stereo Matching for High Quality
578 Digital Elevation Models. *PFG Photogrammetrie-Fernerkundung-*
579 *Geoinformation*, 2012(4), pp. 331-343. DOI: 10.1127/1432-8364/2012/0121
580 Hergarten, S. (2003). Landslides, sandpiles, and self-organized criticality. *Natural*
581 *Hazards and Earth System Sciences*, 3(6), pp. 505–514. DOI: 10.5194/nhess-
582 3-505-2003
583 Hovius, N., Stark, C., & Allen, P. (1997). Sediment flux from a mountain belt derived
584 by landslide mapping. *Geology*, 25(3), pp. 231–234. DOI: 10.1130/0091-
585 7631(1997)025<0231:SFFAMB>2.3.CO;2
586 Hovius, N., Stark, C., Hao-Tsu, C., & Jiun-Chuan, L. (2000). Supply and removal of
587 sediment in a landslide-dominated mountain belt: central range, Taiwan.
588 *Journal of Geology*, 108, pp. 73–89.
589 Hovius, N., Stark, C., Tutton, M., & Abbott, L. (1998). Landslide-driven drainage
590 network evolution in pre-steady-state mountain belt: Finisterre Mountains,
591 Papua New Guinea. *Geology*, 26(12), pp. 1071–1074. DOI: 10.1130/0091-
592 7613(1998)026<1071:LDDNEI>2.3.CO;2
593 Hugenholtz, C. H., Whitehead, K., Brown, O. W., Barchyn, T. E., Moorman, B. J.,
594 LeClair, A., Riddell, K., & Hamilton, T. (2013). Geomorphological mapping with
595 a small unmanned aircraft system (sUAS): Feature detection and accuracy

596 assessment of a photogrammetrically-derived digital terrain model.
597 *Geomorphology*, 194, pp. 16-24. DOI:10.1016/j.geomorph.2013.03.023
598 Korup, O. (2005). Distribution of landslides in southwest New Zealand. *Landslides*,
599 2(1), pp. 43–51. DOI: 10.1007/s10346-004-0042-0
600 Leake, J., Wolf, J., Lowe, J., Hall, J., & Nicholls, R. (2009). 'Response of marine
601 climate to future climate change: application to coastal regions.' in McKee
602 Smith, J. (Ed.) *Proceedings of the 31st International Conference on Coastal*
603 *Engineering*, pp. 4354-4364.
604 Lee, E. M., Hall, J. W., & Meadowcroft, I. C. (2001). Coastal cliff recession: the use
605 of probabilistic prediction methods. *Geomorphology*, 40(3-4), pp. 253-269.
606 DOI: 10.1016/S0169-555X(01)00053-8
607 Lim, M., Rosser, N. J., Allison, R. J., & Petley, D. N. (2010). Erosional processes in
608 the hard rock coastal cliffs at Staithes, North Yorkshire. *Geomorphology*, 114(1-
609 2), pp. 12-21. DOI: 10.1016/j.geomorph.2009.02.011
610 Lowe, J.A., Howard, T., Pardaems, A., Tinker, J., Holt, J., Wakelin, S., Milne, G.,
611 Leake, J., Wolf, J., Horsburgh, K., Reeder, T., Jenkins, G., Ridley, J., Dye, S., &
612 Bradley, S. (2009). *UK Climate Projections science report: Marine and coastal*
613 *projections*. Exeter, UK: Met Office Hadley Centre.
614 Malamud, B., Turcotte, D., Guzzetti, F., & Reichenbach, P. (2004). Landslide
615 inventories and their statistical properties. *Earth Surface Processes and*
616 *Landforms*, 29(6), pp. 687–711. DOI: 10.1002/esp.1064
617 Marques, F.M.S.F. (2008). Magnitude–frequency of sea cliff instabilities. *Natural*
618 *Hazards and Earth System Sciences,* 8(5), pp. 1161–1171. DOI:
619 10.5194/nhess-8-1161-2008

620 Martin, Y., Rood, K., Schwab, J., & Church, M. (2002). Sediment transfer by shallow
621 landsliding in the Queen Charlotte Islands, British Columbia. *Canadian Journal*
622 *of Earth Sciences*, 39(2), pp. 189–205. DOI: 10.1139/e01-068
623 May, V. J. (2003) – 'Beachy Head – Seaford Head Chapter 4: Soft Rock Cliffs' in
624 May, V. J., & Hansom, J. D. *Coastal Geomorphology of Great Britain.*
625 *Geological Conservation Review Series, No. 28*. Peterborough: Joint Nature
626 Conservation Committee, 10.
627 Mitchell, S.B., & Pope, D.J. (2004). 'Prediction of nearshore wave energy distribution
628 by analysis of numerical wave model output: East Sussex coastline, UK', in
629 Mortimore, R. N., & Duperret, A. (Eds.) *Coastal Chalk Cliff Instability*. London:
630 Geological Society, Engineering Geology Special Publications, pp. 99-108.
631 Moore, J. R., Sanders, J. W., Dietrich, W. E., & Glaser, S. D. (2009). Influence of
632 rock mass strength on the erosion rate of alpine cliffs. *Earth Surface Processes*
633 *and Landforms*, 34(10), pp. 1339-1352. DOI: 10.1002/esp.1821
634 Moore, R., Fish, P., Koh, A., Trivedi, D., & Lee, A. (2003a). Coastal change analysis:
635 a quantitative approach using digital maps, aerial photographs and LiDAR.
636 *Proceedings of the International Conference on Coastal Management,*
637 *Brighton*, pp197-211.
638 Moore, R., Fish, P. Glennerster, M., & Bradbury, A. (2003b). Cliff behaviour
639 assessment: a quantitative approach using digital photogrammetry and GIS.
640 *Proceedings of the 38th DEFRA Conference of River and Coastal Engineers*,
641 pp08.3.1-08.3.13.
642 Mortimore, R. N. (1997). *The Chalk of Sussex and Kent*. London: The Geologists
643 Association.

644 Mortimore, R. N., Lawrence, J., Pope, D., Duperret, A., & Genter, A. (2004a).
645 'Coastal cliff geohazards in weak rock: the UK Chalk cliffs of Sussex', in
646 Mortimore, R. N., & Duperret, A. (Eds.) *Coastal Chalk Cliff Instability*. London:
647 Geological Society, Engineering Geology Special Publications, pp. 3-32.
648 Mortimore, R. N., Stone, K. J., Lawrence, J., & Duperret, A. (2004b). 'Chalk physical
649 properties and cliff instability', in Mortimore, R. N., & Duperret, A. (Eds.) *Coastal*
650 *Chalk Cliff Instability*. London: Geological Society, Engineering Geology Special
651 Publications, pp. 75-88.
652 Pelletier, J., Malamud, B., Blodgett, T., & Turcotte, D. (1997). Scale-invariance of soil
653 moisture variability and its implications for the frequency-size distributions of
654 landslides. *Engineering Geology*, 48(3-4), pp. 255–268. DOI: 10.1016/S0013-
655 7952(97)00041-0
656 Remondino, F., Barazzetti, L., Nex, F., Scaioni, M., & Sarazzi, D. (2011). UAV
657 Photogrammetry for mapping and 3D modelling – current status and future
658 perspectives. *International Archives of the Photogrammetry, Remote Sensing*
659 *and Spatial Information Sciences, Volume XXXVIII-1/C22, 2011 ISPRS Zurich*
660 *2011 Workshop, 14-16 September 2011, Zurich, Switzerland.*
661 Rossi, M., Witt, A., Guzzetti, F., Malamud, B., & Peruccacci, S. (2010). Analysis of
662 historical landslide time series in the Emilia-Romagna region, northern Italy.
663 *Earth Surface Processes and Landforms*, 35(10), pp. 1123–1137. DOI:
664 10.1002/esp.1858
665 Selby, M. J. (Ed.) (1993). *Hillslope materials and processes* (2nd edn.). Oxford:
666 Oxford University Press.
667 Slatton, K. C., Carter, W .E., Shrestha, R. L., & Dietrich, W. (2007). Airborne laser
668 swath mapping: achieving the resolution and accuracy required for geosurficial

669 research. *Geophysical Research Letters*, 34, p. L23S10. DOI:
670 10.1029/2007GL031939
671 Stark, C., & Guzzetti, F. (2009). Landslide rupture and probability distribution of
672 mobilized debris volumes. *Journal of Geophysical Research*, 114(F2), pp.
673 F00A02. DOI: 10.1029/2008JF001008
674 Stark, C., & Hovius, N. (2001). The characterization of landslide size distributions.
675 *Geophysical Research Letters*, 28(6), pp. 1091–1094. DOI:
676 10.1029/2000GL008527
677 Stead D., & Coggan J. (2012). Numerical modeling of rock slope instability. In:
678 Clague J.J. & Stead D. (eds) Landslides Types, Mechanisms and Modelling,
679 pp. 144-158.
680 Sunamura, T. (2015). Rocky coast processes: with special reference to the
681 recession of soft rock cliffs. *Proceedings of the Japan Academy, Series B*,
682 91(9), pp. 481-500. DOI: 10.2183/pjab.91.481
683 Teixeira, S.B. (2006). Slope mass movements on rocky sea cliffs: a power-law
684 distributed natural hazard on the Barlavento Coast, Algarve, Portugal.
685 *Continental Shelf Research,* 26(9), pp. 1077–1091. DOI:
686 10.1016/j.csr.2005.12.013
687 Thieler, E. R., Himmelstoss, E. A., Zichichi, J. L., & Ergul, A. (2009). *Digital Shoreline*
688 *Analysis System (DSAS): An ArcGIS extension for calculating shoreline change*
689 *(Version 4.0) [Computer software]. U.S. Geological Survey Open-File Report*
690 *2005-1304.* Retrieved from: https://woodshole.er.usgs.gov/project-
691 pages/DSAS/version4/index.html (link may change with updates to software –
692 link to all versions is https://woodshole.er.usgs.gov/project-pages/DSAS/)

693 Trenhaile, A. S. (2002). Rock coasts, with particular emphasis on shore platforms.
694 *Geomorphology*, 48(1-3), pp. 7-22. DOI: 10.1016/S0169-555X(02)00173-3
695 United Kingdom Climate Projections (UKCP). (2009). *UK Climate Projections User*
696 *Interface*. Retrieved from: http://ukclimateprojections-
697 ui.metoffice.gov.uk/ui/start/start.php
698 Van Den Eeckhaut, M., Poesen, J., Govers, G., Verstraeten, G., & Demoulin, A.
699 (2007). Characteristics of the size distribution of recent and historical landslides
700 in a populated hilly region. *Earth and Planetary Science Letters*, 256(3-4), pp.
701 588–603. DOI: 10.1016/j.epsl.2007.01.040
702 White, E.P., Enquist, B.J., & Green, J.L. (2008). On estimating the exponent of
703 power law frequency distributions. *Ecology*, 89(4), pp. 905–912. DOI:
704 10.1890/07-1288.1
705 Wolman, M. G., & Miller, J. P. (1960). Magnitude and frequency of forces in
706 geomorphic processes. *Journal of Geology*, 68(1), pp. 54-74. DOI:
707 10.1086/626637
708 Wong, P.P., Losada, I.J., Gattuso, J.-P., Hinkel, J., Khattabi, A., McInnes, K.L.,
709 Saito, Y., & Sallenger, A. (2014). Coastal systems and low-lying areas, in Field,
710 C.B., Barros, V.R., Dokken, D.J., Mach, K.J., Mastrandrea, M.D., Bilir, T.E.,
711 Chatterjee, M., Ebi, K.L., Estrada, Y.O., Genova, R.C., Girma, B., Kissel, E.S.,
712 Levy, A.N., MacCracken, S., Mastrandrea, P.R., & White, L.L. (eds.) *Climate*
713 *Change 2014: Impacts, Adaptation, and Vulnerability. Part A: Global and*
714 *Sectoral Aspects. Contribution of Working Group II to the Fifth Assessment*
715 *Report of the Intergovernmental Panel on Climate Change*. Cambridge
716 University Press, Cambridge, United Kingdom and New York, NY, USA, pp.
717 361-409.

718